Journal of Power Sources 202 (2012) 314–321

Contents lists available at SciVerse ScienceDirect

Journal of Power Sources

journal homepage: www.elsevier.com/locate/jpowsour

Structural and electrochemical properties of $LiMoO_2$

K. Ben-Kamel[a], N. Amdouni[a], H. Groult[b], A. Mauger[c], K. Zaghib[d], C.M. Julien[b,*]

[a] Université Tunis-El Manar, U.R. Physico-Chimie des Matériaux Solides, 1060 Tunis, Tunisia
[b] Université Pierre et Marie Curie-Paris-6, Laboratoire des Electrolytes, Colloïdes et Systèmes Analytiques (PECSA), 4 place Jussieu, 75005 Paris, France
[c] Université Pierre et Marie Curie-Paris-6, Institut de Minéralogie et Physique de la Matière Condensée (IMPMC), 4 place Jussieu, 75005 Paris, France
[d] Institut de Recherche d'Hydro-Québec, 1800 Bd Lionel-Boulet, Varennes, Québec, Canada J3X 1S1

ARTICLE INFO

Article history:
Received 24 October 2011
Received in revised form
18 November 2011
Accepted 19 November 2011
Available online 27 November 2011

Keywords:
Lithium secondary batteries
Lithium molybdenum oxides
Lattice dynamics
Lithium diffusivity

ABSTRACT

In this paper, we revisit the structural and electrochemical properties of lithium molybdenate, $LiMoO_2$, synthesized by a carbothermal method using citric acid as a chelating agent. Free-impurity microcrystalline powders were grown by a two-step synthesis with a final thermal treatment at 800 °C for 72 h in air. $LiMoO_2$ was characterized by means of X-ray diffractometry (XRD), Fourier transform infrared (FTIR) and Raman scattering (RS) spectroscopy and by nuclear magnetic resonance (NMR). Analyzing the data from the above experiments, we determine that $LiMoO_2$ crystallizes in the monoclinic system ($C2/m$ S.G.) instead of the rhombohedral structure ($R\bar{3}m$ S.G.) such as reported previously. The electrochemical performance of the synthesized products was evaluated in Li cells using non-aqueous solution 1 mol L^{-1} $LiPF_6$ in EC–DMC as electrolyte. The charge–discharge profiles of the monoclinic-phase $LiMoO_2$ display two plateaus and show the suitability of this electrode for electrochemical applications delivering a specific capacity 185 mAh g^{-1} in the potential range 3.7–2.0 V vs. Li^0/Li^+. The chemical diffusion coefficient of Li^+ ions into the $LiMoO_2$ framework has been studied as a function of Li concentration; results show values in the range 10^{-11}–10^{-12} cm^2 s^{-1}.

1. Introduction

Layered compounds with a layered framework are the dominant cathode materials used presently in Li-ion batteries, because Li^+ ions can be electrochemically extracted and inserted with high reversibility [1,2]. Most $LiMO_2$ oxides (M = transition metal) are related to the rock-salt structure and are either ordered or distorted forms of NaCl. One possibility, exemplified by $LiInO_2$, is a 1:1 ordering on the cation sites, which reduces the space group symmetry from O_h^5 ($Fm3m$ structure) to a tetragonal D_{4h}^{19} ($I41/amd$ space group with $Z = 3$). The second possibility is a distortion of NaCl consisting of an elongation of the unit cell along the (1 1 1) direction; the space group is $R\bar{3}m$ with $Z = 1$. This arrangement is sometimes known as either the $NaHF_2$-type structure or the α-$NaFeO_2$-type structure. $LiCoO_2$ and $LiNiO_2$ belong to this class, but the later compound exists in a Jahn–Teller distorted variant with cationic disorder between lithium and nickel ions. A third structure γ-$LiAlO_2$, which is not related to rock salt, consists of corner-linked tetrahedra in which both Li and Al are four-coordinated. Some compounds present metastable low-temperature modification, such as $LiMnO_2$. The lower symmetry of the layered $LiMnO_2$ phase compared with $LiCoO_2$ was associated with the strong Jahn–Teller effect for Mn^{3+} ions. [3–5].

Numerous molybdenum oxides have been identified as lithium insertion compounds for using as positive electrodes in rechargeable lithium batteries [6–10]. Among the varieties of Mo–O compounds, hydrated phases MoO_3–nH_2O have shown voltages lower than for the polycrystalline phase due to the partial reduction of Mo^{6+} ions in the highly disordered phase [11].

Considering the Li–Mo–O phase diagram (Fig. 1) various phases appear to be stable in the triangle MoO_2–Li–MoO_3 including $LiMoO_2$, Li_2MoO_3, $Li_4Mo_3O_8$ and $Li_{0.74}MoO_2$. As pointed out by Hibble et al. [12] these phases have closely related structures, and a notable feature is that the cell metrics of $LiMoO_2$ and $Li_4Mo_3O_8$ differ very little.

There were few reports on the structure, physico-chemical properties and electrochemistry of $LiMoO_2$ [13,14]. However, its structure has been the subject of debate. Several groups have claimed that $LiMoO_2$ crystallizes with the rock-salt-like structure isomorphs to the layered α-$NaFeO_2$ [13–16]. These groups did not consider the accepted theoretical predictions for 3D-systems according to which the structure would distort, while Hibble et al. [12] have determined that $LiMoO_2$ adopts the monoclinic $C2/m$ space group (S.G.) by refinement of by neutron scattering data. Because the controversy seems to originate from an incorrect analysis of X-ray diffraction (XRD) data and the absence of proper Rietveld refinements, we decided to reconsider the true structure

* Corresponding author.
E-mail address: christian.julien@upmc.fr (C.M. Julien).

0378-7753/$ – see front matter © 2011 Elsevier B.V. All rights reserved.
doi:10.1016/j.jpowsour.2011.11.061

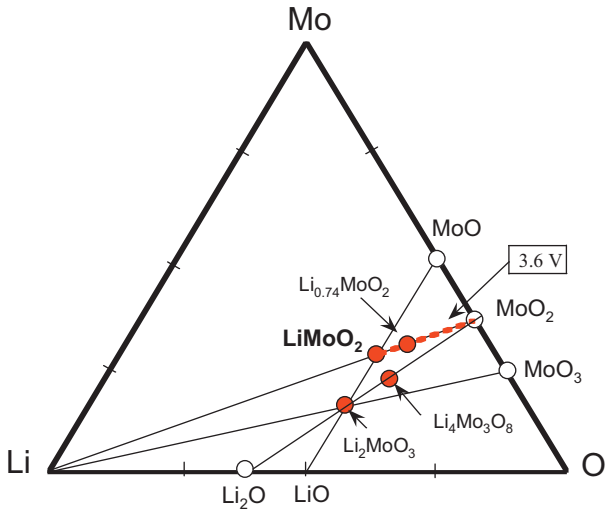

Fig. 1. Phase diagram of the Li–Mo–O system.

of $LiMo^{III}O_2$ synthesized by an identical method that was used by Barker et al. [14] for easy comparison.

The purpose of this paper is threefold. First, we carried out the X-ray diffraction (XRD) of $LiMoO_2$ powders prepared by a two-step synthesis, and we investigated its structure using Rietveld refinement in both crystallographic systems, i.e. the hexagonal $R\bar{3}m$ and the monoclinic $C2/m$ symmetry. Second, we investigated the intrinsic properties of the local structure of $LiMoO_2$ using experiments that provide the fingerprints of the materials, namely optical spectroscopy including Fourier transform infrared (FTIR) and Raman scattering (RS), and nuclear magnetic resonance (NMR). As vibrational spectroscopy is very effective in identifying the symmetry of condensed matter especially the local structure of solids, FTIR and RS have left the ambiguity met during the determination of complex structures. An example was supplied by the case of the low temperature form of $LiCoO_2$ which crystallizes in the spinel structure instead of the α-$NaFeO_2$-like polymorph [17]. Finally, we present the electrochemical properties of $LiMo^{III}O_2$ by coupling it as a positive electrode with a Li anode in a non-aqueous $LiPF_6$–EC–DMC (1:1) electrolyte.

2. Experimental

2.1. Synthesis

To ensure the same conditions of preparation, the synthesis of $LiMoO_2$ was performed using the two-step process reported by Barker et al. [14]. This is the condition to obtain identical specimens for a direct comparison of structural features. The first step consists in an carbothermal process in which Mo(VI) from molybdic acid is reduced to $Mo^{IV}O_2$ using graphitized carbon. The MoO_3 monohydrate was mixed and ground with the stoichiometric amount of carbon followed by heat treatment at 750 °C during 12 h using a tubular furnace into flowing Ar ambient. MoO_2 powders were formed according the reaction

$$MoO_3{-}H_2O + C \rightarrow MoO_2 + H_{2\uparrow} + CO_{2\uparrow} \quad (1)$$

After a slow cooling down, the structure and purity of MoO_2 products was verified by XRD with the $P2_1/c$ space group, file ASTM 78-10130 [18]. The second step consists in the reduction of Mo(IV) to Mo(III) by mixing and heating the by-product with stoichiometric amounts of lithium carbonate at moderate temperature 600 °C for 72 h. Note the careful control of the temperature in this second step is required, because the product decomposes above 600 °C. On another hand, calcination below 600 °C leads to worse structural properties and less integrity of the lattice. The 72-h duration is dictated by the fact that the solid-state reaction is a slow process. No further improvement could be detected by increasing the heating time above 600 °C. The final material is obtained according the relation

$$Li_2CO_3 + 2MoO_2 \rightarrow 2LiMoO_2 + CO_{\uparrow} + (1/2)O_{2\uparrow} \quad (2)$$

Note that the synthesis of $LiMoO_2$ occurs by solid-state reaction, not by the carbothermal process envisioned by Barker et al. [14]. Actually, carbothermal reduction of MoO_3 is possible, but only at very high temperature in the range 1100–1400 °C [19]. Since, however, $LiMoO_2$ decomposes above 600 °C, the synthesis of $LiMoO_2$ by carbothermal reduction is impossible. On another hand, the insertion of Li into oxides of transition metals by solid-state reaction between them and lithium carbonate at lower temperature is not restricted to the case of molybdenum. It has been successfully achieved for instance in the case of cobalt, since Antolini has synthesized $LiCoO_2$ by this process, i.e. by heating $Li_2Co_3 + Co_3O_4$ at 380 °C [20,21].

2.2. Sample characterization

The XRD diagrams were obtained on a Philips X'Pert PRO MRD (PW3050) diffractometer equipped with a Cu anticathode (CuK_α radiation $\lambda = 1.54056$ Å) at room temperature. The measurements have been recorded under Bragg-Brentano geometry at 2θ with step 0.05° in the range 10–80°. The surface morphology was analyzed by means of scanning electron microscopy (SEM) using a Philips XL300 instrument. FTIR absorption spectra were recorded using a Bruker IFS113v interferometer at a spectral resolution 2 cm^{-1}. In the studied region (100–700 cm^{-1}), this vacuum bench apparatus was equipped with a 3.5-μm thick beamsplitter, a globar source, and a DTGS-PE far-infrared detector. Samples were ground to fine powders painted onto polyethylene slab which is a transparent substrate in the studied spectral range. Raman spectra were measured using a Jobin-Yvon U1000 double pass spectrometer equipped with a cooled, low noise photomultiplier tube (ITT FW130). The incident light used for the experiments was the 515 nm Ar line of a laser source. The ^{7}Li MAS NMR experiments were carried out at 116.6 MHz using a Bruker model-300 spectrometer. The ^{7}Li chemical shifts were externally referenced to LiCl (1 M) at 0.0 ppm.

2.3. Electrochemical measurements

Electrochemical measurements were made using a laboratory-scale Li//$LiMoO_2$ cells housed in a Teflon laboratory-cell hardware employing a non-aqueous Li^+ ion conducting organic electrolyte as follows. The electrolyte was prepared by dissolving 1 M $LiPF_6$ in ethylene–dimethylene carbonate (EC–DMC) mixture. The cathode-active materials (~9 mg) were pressed onto an expanded aluminium microgrid at a pressure of 500 MPa. This procedure yields circular pellet electrodes of 10 mm diameter. The pellets were then dried at 120 °C in air. Glass paper soaked in electrolyte was used as the membrane separator between the cathode and the anode. Electrochemical measurements were carried out using a Mac-Pile system in the galvanostatic mode. Quasi open-circuit voltage profiles were measured using intermittent charging as follows. A current of 0.14 mA cm^{-2} was supplied for 1 h, corresponding to a lithium extraction of about 0.01 mole from 1 mole of the electrode material. This was followed by a relaxation time of 0.5 h before the next charging started. The charging–discharging processes were monitored in the potential range between 2.0 and 3.7 V, corresponding to a depth-of-discharge (DOD) of $\Delta x \approx 0.9$. The lithium

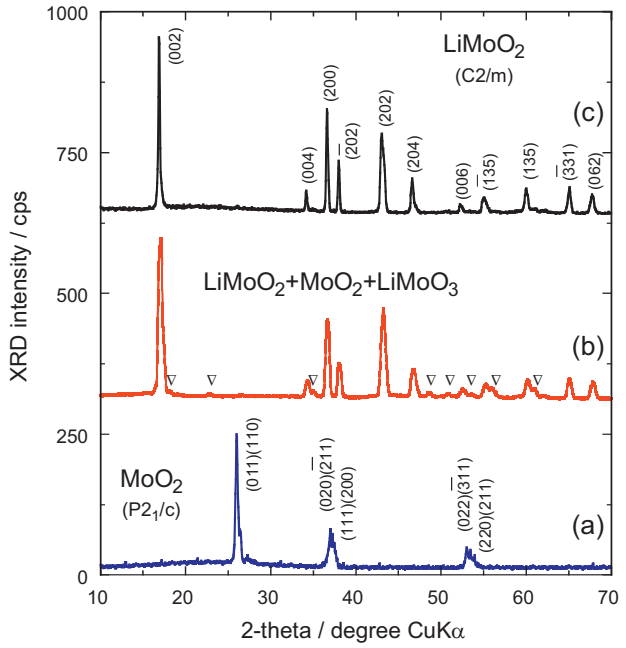

Fig. 2. XRD patterns of products obtained for the synthesis of $LiMoO_2$. (a) First-step MoO_2, (b) second-step intermediate material, and (c) final product. The symbols in (b) point to the peaks associated to MoO_2 and $LiMoO_3$ impurities, detected at the second step of the synthesis only.

content of the charge–discharge compounds was estimated from the current through the cell and the mass of the electrode material.

3. Results and discussion

3.1. Structure and morphology of $LiMoO_2$ grains

Fig. 2 (curves a–c) shows three XRD patterns recorded during the two-step synthesis of $LiMoO_2$ powders. The diagram (curve a) representing the XRD pattern of the first-step product $Mo^{IV}O_2$ has been indexed with the monoclinic system $P2_1/c$ space group. The XRD pattern of the intermediate second-step $LiMo^{III}O_2$ obtained after heating at 600 °C for 12 h is shown in curve b. Finally, the XRD spectrum of well-crystallized $LiMoO_2$ calcined at 600 °C for 72 h is displayed in Fig. 2c. The XRD peaks gradually sharpen with increasing firing duration, which indicates a better crystallinity that may occur from growth of grain size, ordering of local structure, and/or release of impurity. Note that 600 °C is the optimum temperature for calcination, since higher temperature results in the decomposition of the material. After heating at 600 °C for 12 h only, we have identified the presence of impurities such as MoO_2 and $LiMoO_3$. An impurity free $LiMoO_2$ compound is formed after heating during 72 h. The corresponding XRD diagram is dominated by the Bragg line at $2\theta = 16.9°$ corresponding the planar distance 5.242 Å; lines with medium intensity are observed at ca. $2\theta = 36.5$, 38.0, 43.0 and 46.6°.

To discriminate the actual Mo-O-Mo bonding in $LiMoO_2$, we consider the two possible crystallographic systems reported previously, namely the rhombohedral structure ($R\bar{3}m$ S.G.) described by Aleandri and McCarly [15] and the monoclinic structure ($C2/m$ S.G.) reported by Hibble et al. [12]. Both of them are illustrated in Fig. 3, and correspond to a $LiMoO_2$ lattice formed by distorted MoO_6 octahedral units to allow the formation of zig-zag chains. Fig. 4 shows the Rietveld refinements in these two geometries. The refined lattice and atomic parameters are given in Tables 1 and 2. The crystallographic parameters for the rhombohedral $LiMoO_2$ (in hexagonal setting) are found to be $a = 2.867(7)$ Å and $c = 15.499(4)$ Å,

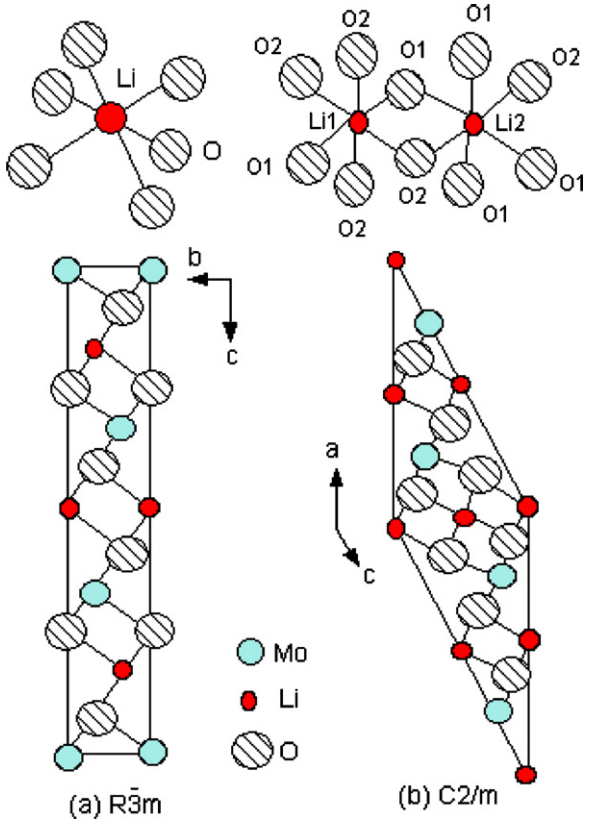

Fig. 3. Schematic representation of the rhombohedral and monoclinic structures of $LiMoO_2$.

Table 1
Rietveld refinement of XRD patterns for LiMoO2 using the $C2/m$ space group, taking full occupancy of each crystallographic position as constraints.

Atom	Site	Wyckoff positions			β_{iso}(Å^2)
Li(1)	2*c*	1/2	1/2	1/2	2.1
Li(2)	2*a*	0	0	0	2.1
Mo	4*i*	0.4865	0	0.2419	1.4
O(1)	4*i*	0.3193	0	1.0094	0.5
O(2)	4*i*	0.6993	0	0.5623	0.5

Lattice parameters: $a = 10.651(2)$ Å, $b = 2.876(4)$ Å, $c = 10.995(1)$ Å, $\beta = 153.51°$
Profile parameters-Pseudo-Voigt function: $PV = \eta L + (1-\eta)G - \eta = 0.039$
Conventional Rietveld *R*-factors for points with Bragg contribution
Halfwidth parameters: $U = 2.073$; $V = -1.60$; $W = 0.575$
$R_p = 9.79\%$; $R_{wp} = 8.99\%$; $R_F = 2.49\%$; $R_{Bragg} = 1.24\%$; $\chi^2 = 1.33$

Table 2
Rietveld refinement of XRD patterns for $LiMoO_2$ using the $R\bar{3}m$ space group, taking full occupancy of each crystallographic position as constraints.

Atom	Site	Wyckoff positions			β_{iso}(Å^2)
Li	3*b*	0	0	0	1.5
Mo	3*a*	0	0	1/2	1.2
O	6*c*	0	0	0.267	0.8

Lattice parameters: $a = 2.867(7)$ Å; $b = 2.867(2)$ Å; $c = 15.699(4)$ Å
Profile parameters
Conventional Rietveld *R*-factors for points with Bragg contribution
Pseudo-Voigt function: $PV = \eta L + (1-\eta)G - \eta = 0.104$
$R_p = 16.6\%$; $R_{wp} = 16\%$; $R_F = 10.28\%$; $R_{Bragg} = 8.53\%$; $\chi^2 = 3.32$
Halfwidth parameters: $U = 1.461$; $V = -0.625$; $W = 0.319$

while the monoclinic structure gives $a = 10.651(2)$ Å, $b = 2.876(4)$ Å, $c = 10.995(1)$ Å and $\beta = 153.51°$.

As observed in the figure, both systems work quite well to refine XRD patterns but a close examination indicates that the monoclinic system is a better model for the structure of $LiMoO_2$. The refinement

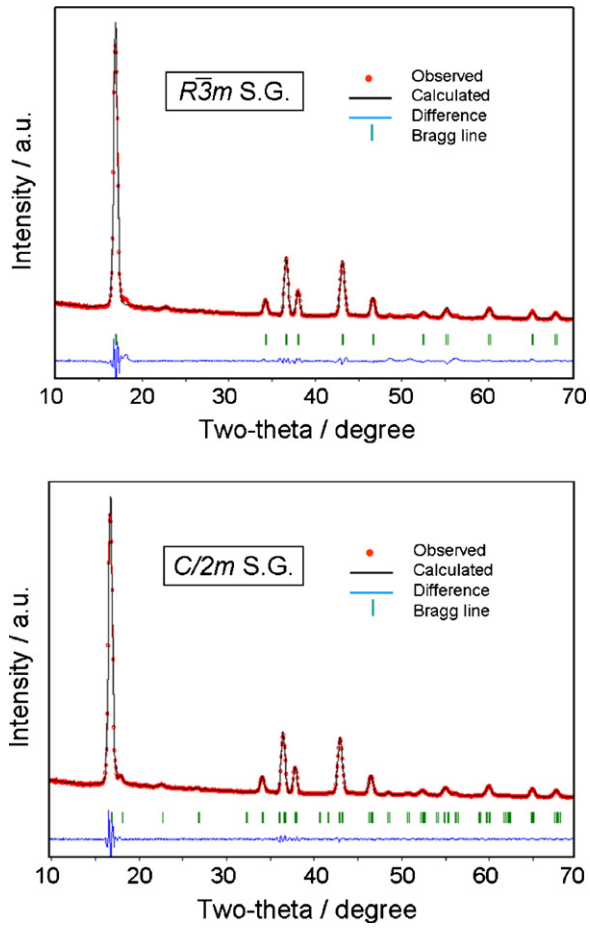

Fig. 4. Rietveld refinements of XRD patterns of $LiMnO_2$ using the hexagonal $R\bar{3}m$ symmetry (a) and the monoclinic $C2/m$ symmetry.

with a strict two-dimensional structure ($R\bar{3}m$ S.G.) corresponding to $[Li]_{3b}(Mo)_{3a}[O_2]_{6c}$ reveals that the thermal parameter of Li, β_{Li}, is smaller than the value obtained with the refinement in the framework of the monoclinic structure ($C2/m$ S.G.), for which the structural model is $[Li(1)_{2c}Li(2)_{2a}](Mo)_{4i}[O_2]_{4i}$. The Rietveld refinements led to R_{Bragg} = 1.24% for the monoclinic system, while higher value R_{Bragg} = 8.53% is obtained for the rhombohedral system. Therefore, the better refinement obtained within the monoclinic system pleads in favour of this structure for $LiMoO_2$. This statement will be verified in the following by the analysis for the lattice dynamics investigated by FTIR and Raman spectroscopy because these techniques, sensitive to the local symmetry of the structure, display a strong difference between the vibrational modes of the rhombohedral framework versus the monoclinic one.

Fig. 5 shows the typical scanning micrographs of $LiMoO_2$ samples fired at 600 °C in air for 72 h. These pictures reveal that the gel precursors fired at 600 °C develop well-crystallized samples with homogeneous morphologies. The specific synthetic process results in grains with elongated shape. An average size below 0.5 μm × 0.8 μm was obtained with a fairly narrow grain size distribution range. The grains are almost connected and ensure high surface area. Note that the introduction of the carbon in the initial step of the synthesis of the samples does not affect the morphology of the $LiMoO_2$ samples.

According to the Scherrer law, the width of the XRD lines is inversely proportional to the coherent length L of the crystallites using the formula

$$L = \frac{0.9\lambda}{B\cos\theta} \quad (3)$$

Table 3
Factor group analysis for $LiMoO_2$ zigzag chain structure (C_{2h}^3 symmetry).

Atom	Wyckoff position	Site group	Irreducible representation
Mo	4*i*	C_s	$A_g \oplus B_g \oplus A_u \oplus B_u$
O(1)	4*i*	C_s	$A_g \oplus B_g \oplus A_u \oplus B_u$
O(2)	4*i*	C_s	$A_g \oplus B_g \oplus A_u \oplus B_u$
Li(1)	2*c*	C_{2h}	$A_u \oplus B_u$
Li(2)	2*a*	C_{2h}	$A_u \oplus B_u$
Total			$3A_g \oplus 3B_g \oplus 5A_u \oplus 5B_u$
Acoustic			$A_u \oplus B_u$
Raman			$3A_g \oplus 3B_g$
Infrared			$4A_u \oplus 4B_u$

Table 4
Determination of the infrared- and Raman active modes for $LiMoO_2$ (C_{2h}^3 spectroscopic symmetry).

	Number of modes						Spectral activity
Species C_{2h}	Mo C_s	O(1) C_s	O(2) C_s	Li(1) C_{2h}	Li(2) C_{2h}	Total	
A_g	1	1	1	–	–	3	$\alpha_{xx}, \alpha_{yy}, \alpha_{zz}, \alpha_{xy}$
B_g	1	1	1	–	–	3	α_{xz}, α_{yz}
A_u	1	1	1	1	1	5	T_z
B_u	1	1	1	1	1	5	T_x, T_y
Acoustic modes $1A_u + 1B_u$							
Optical active modes $3A_g + 3B_g + 4A_u + 4B_u$							

where B is the full width at the half maximum (fwhm) of the XRD line and λ is the XRD wavelength in Å. The value 21 nm and 16 nm is found for L in the (0 0 2) and the (2 0 0) direction, respectively, which means that the $LiMoO_2$ grains are made of several crystallites.

3.2. Spectroscopic investigations

Since the determination of the symmetry was difficult to differentiate from XRD pattern, both FTIR and Raman scattering (RS) experiments turned out to be determinant in the debate on the structure of $LiMoO_2$. Indeed, these techniques are probes of the local structure. Let to discuss first the factor group analysis of $LiMO_2$ oxides [22–24].

The $LiMO_2$ (M = Ni, Cr, Co) oxides adopt the α-$NaFeO_2$-type layered structure that belong to the crystallographic $R\bar{3}m$ space group have a corresponding spectroscopic D_{3d}^5 spectroscopic symmetry. This structure derives from the NaCl structure with a stacking of Li ions between adjacent MO_2 slabs. The M cations are located in octahedral 3*a* (0 0 0) sites and oxygen anions are in a cubic close-packing, occupying the 6*c* (0 0 *z*, 0 0 *z*) sites. Li cations reside at Wyckoff 3*b* (0 0 1/2) sites. The transition metal and lithium ions are occupying the alternating (1 1 1) planes. The Bravais cell contains one molecule (Z = 1). The infrared (ir)- and Raman (R)-active modes have been determined and discussed elsewhere [19]. They are given by the species $1A_g(R) + 1E_g(R) + 2A_{2u}(ir) + 2E_{2u}(ir)$ in the D_{3d}^5 spectroscopic symmetry

In the monoclinic model ($C2/m$ S.G.), the molybdenum ions and the oxygen anions occupy the 4*i* sites, while lithium ions are located in 2*c* (1/2, 1/2, 1/2) and 2*a* (0 0 0) sites [12]. The Bravais cell contains two molecules (Z = 2). The corresponding site symmetry of the C_{2h}^3 space group containing both the infrared and Raman active modes is given by [20]

$$4C_{2h}(1),\ 2C_i(2),\ 2C_2(2),\ C_s(2),\ C_1 \quad (4)$$

where each site-group symbol is preceded by an integer indicating the number of distinct sites of each symmetry, followed by the multiplicity in parentheses. By factor group analysis, one obtains the reduction in irreducible representations (Tables 3 and 4). According to the factor group analysis, the monoclinic $LiMoO_2$ is predicted to

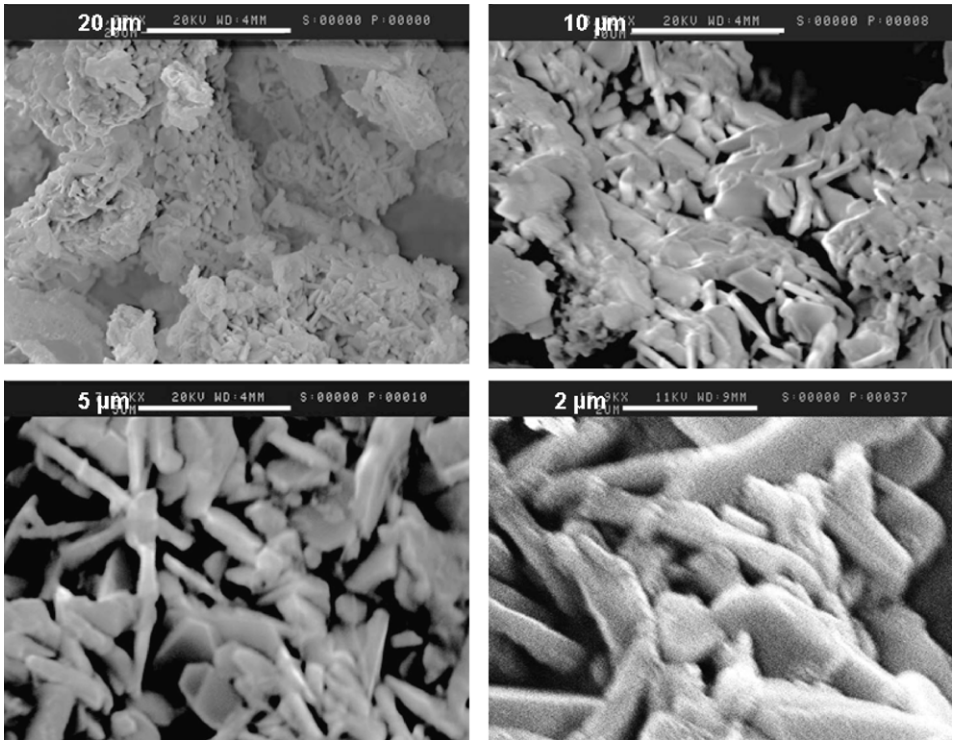

Fig. 5. SEM images of microcrystalline $LiMoO_2$ grown by solid-state synthesis.

show 6 Raman-active modes with $3A_g + 3B_g$ species and 8 IR-active modes with $4A_u + 4B_u$ species based on the polyhedron coordination around the Mo^{3+} cations.

Fig. 6a shows the FTIR absorption spectrum of $LiMoO_2$ powders fired at 600 °C. Note that the multiplicity of IR and Raman bands is due to the irregular Mo–O interatomic distance in the $LiMoO_2$ lattice. Hibble et al. [12] have reported seven types of Mo–O bonds in the $C2/m$ model instead of two types in the $R\bar{3}m$ model. The FTIR absorption spectrum displays features that can be divided into three parts: (i) in the high-wavenumber region, bands are asymmetric stretching modes of Mo–O bonds with the octahedral coordination which has broken into several distinct components due to multiplicity of interatomic distance, (ii) the bands in the range 350–600 cm^{-1} are bending modes involving O–Mo–O symmetric and antisymmetric modes and (iii) the low-wavenumber region in which an isolated strong band is centered at ca. 260 cm^{-1} is attributed to the lithium cage mode. These features are different than those of $LiMO_2$ (M = Ni, Co) compounds for which less number of modes are observed [19], thus confirming the monoclinic structure determined by XRD.

Fig. 6b shows the Raman scattering spectrum of $LiMoO_2$ powders fired at 600 °C. The RS features prove that the symmetry is monoclinic, with twelve bands instead of the two ($1A_{1g} + 1E_g$) for the rhombohedral one [19]. The high-frequency peak located at 895 cm^{-1} is assigned to the A_g mode involving the symmetric stretching vibration of equatorial oxygen atoms, while the band at 726 cm^{-1} is attributed to the stretching mode of Mo cations bonded to axial oxygen atoms [21]. The low-frequency peak at 196 cm^{-1} is assigned to the rigid-layer mode with involves two $LiMoO_2$ molecules with the B_g species.

Solid state NMR spectra are strongly affected by the electronic structure of the local environment within the lattice, since Li-NMR spectroscopy is an extremely useful tool for characterizing the local structure in the layered materials, even in highly disordered systems [25–27]. Fig. 7 represents the ^7Li NMR spectrum of $LiMoO_2$. The small value of the hyperfine chemical shift, ca. −0.15 ppm, is

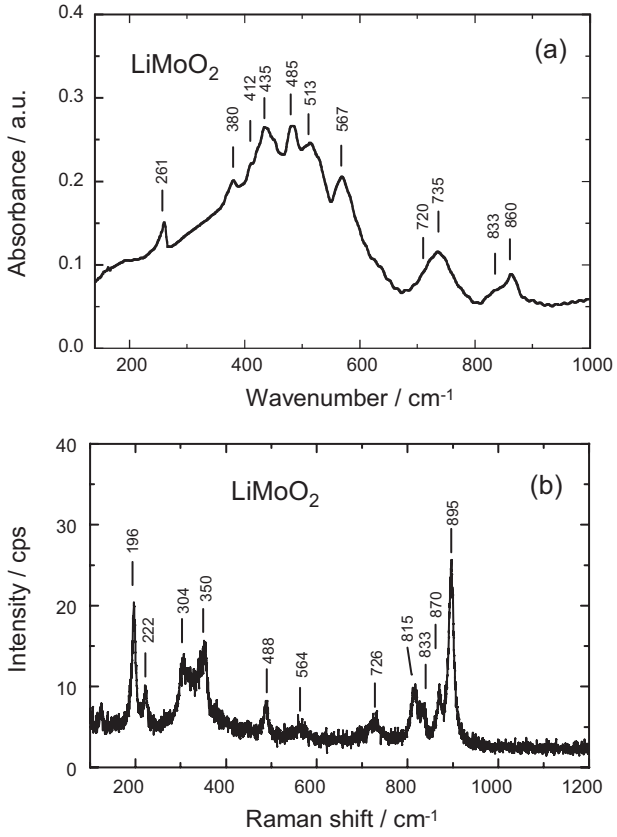

Fig. 6. FTIR (a) and Raman scattering (b) spectra of $LiMoO_2$ powders synthesized by the two-step process. The final product was calcined at 600 °C for 72 h.

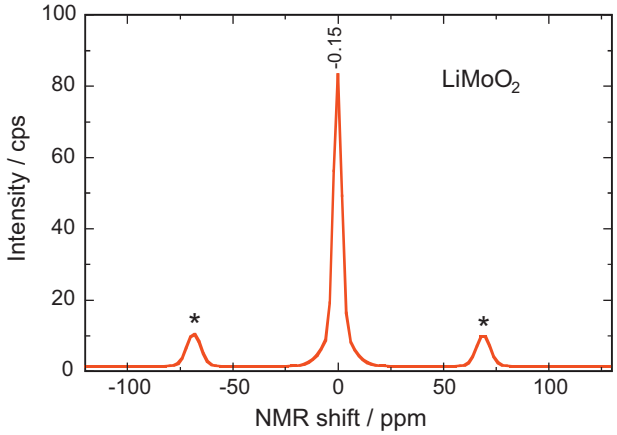

Fig. 7. RMN spectrum of $LiMoO_2$ powders synthesized at 600 °C for 72 h. The spinning side bands are marked with asterisk.

typical for a weak disorder in the first coordination sphere of Mo^{3+} cations, as it represents the spin density transfer from the paramagnetic center of the transition-metal ions to the 2s orbital of the Li^+ nucleus via the intervening 2p oxygen orbitals [25].

The monoclinic symmetry can be understood in the frame of an ionic model as shown in Fig. 8. The plot of the structural stability of a series of $LiMO_2$ oxides is reported as a function of the ionic radius of transition-metal ions $r(M^{3+})$. Materials crystallize in a 3-D structure if $r(M^{3+}) > 0.63$ Å. As $r(Mo^{3+}) = 0.9$ Å [28] is clearly above this critical value, we expect a monoclinic symmetry rather than a 2-D structure for $LiMoO_2$, in agreement with our result.

3.3. Electrochemical studies

Fig. 9 represents the charge–discharge profile of the Li//$LiMoO_2$ cell cycled in the potential range 2–4 V. A current density corresponding to a C-rate as small as C/24 was chosen to evaluate its electrochemical features close to the open-circuit voltage regime. These results indicate that almost 0.9Li can be extracted when the cell was charged at 4.0 V vs. Li^+/Li^0. The curves show a good reversibility at the first cycle with the capacity retention of 168 mAh g^{-1}, which can be compared with the theoretical value 198 mAh g^{-1}. Two regions can be distinguished during the charge: an S-shape potential corresponding to the extraction of 0.5Li in Li_xMoO_2 followed by a plateau at 3.6 V that is attributed to the existence of a two-phase system, i.e. $Li_{0.1}MoO_2$ and $Li_{0.5}MoO_2$.

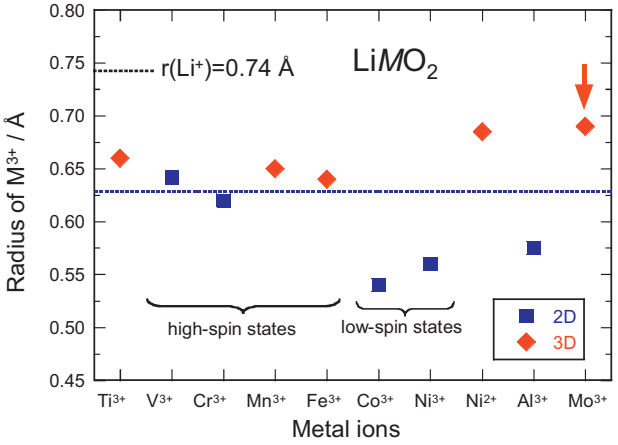

Fig. 8. Plot of the structural stability of $LiMO_2$ oxides as a function of the ionic radius of transition-metal ions.

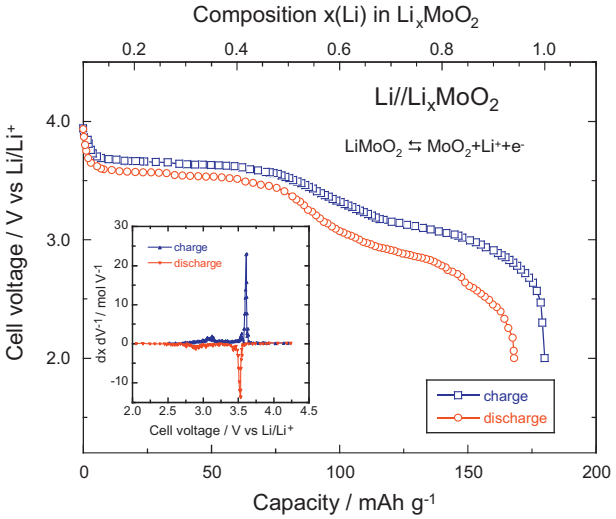

Fig. 9. Charge–discharge profile of the Li//$LiMoO_2$ cell cycled in the potential range 2–4 V at C/24 rate. The electrode was $LiMoO_2$ powders synthesized at 600 °C for 72 h (*C*2/*m* S.G.) and the electrolyte was 1 M $LiPF_6$ in 1:1 EC/DMC. The insert shows the incremental capacity *dQ*/*dV* vs. cell voltage obtained at the second cycle.

The insert (Fig. 9) shows the incremental capacity *dQ*/*dV* vs. cell voltage calculated from the charge–discharge of the first cycle. This graph displays the two sets of peaks that correspond to the extraction/insertion of Li^+ ions from/into the $LiMoO_2$ host matrix, respectively. Each set is related to the two sites occupied by Li ions that are energetically non-equivalent. The sharp peaks at ca. 3.6 V correspond to the voltage plateau observed in the charge–discharge curves. Note that the redox contributions of the single phase regime appear at 2.9 and 3.1 V vs. Li^+/Li^0.

More informative results have been obtained by successive charge–discharge cycles at C/24 rate. Fig. 10 displays electrochemical profiles of the first 17 cycles of the Li//$LiMoO_2$ cell cycled in the potential range 2.0–3.9 V. The insert displays the cycle number dependence of the discharge capacity for the Li//$LiMoO_2$ cell operating in the same conditions. We observed that the reversibility of the Li//Li_xMoO_2 cell decreases rapidly; almost 60% of the initial capacity was lost after 50 cycles. This is attributed to the nature of the monoclinic lattice that favours destabilisation of the structure upon Li^+ extraction. Similar phenomenon has been observed

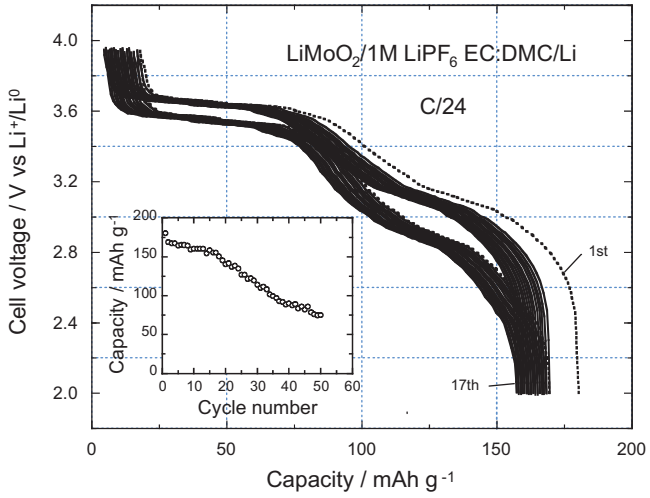

Fig. 10. Charge–discharge profile of the seventeen first cycles of Li//$LiMoO_2$ cell cycled in the potential range 2.0–3.95 V. The insert displays the cycle number dependence of the discharge capacity for the Li//$LiMoO_2$ cell operating at C/24.

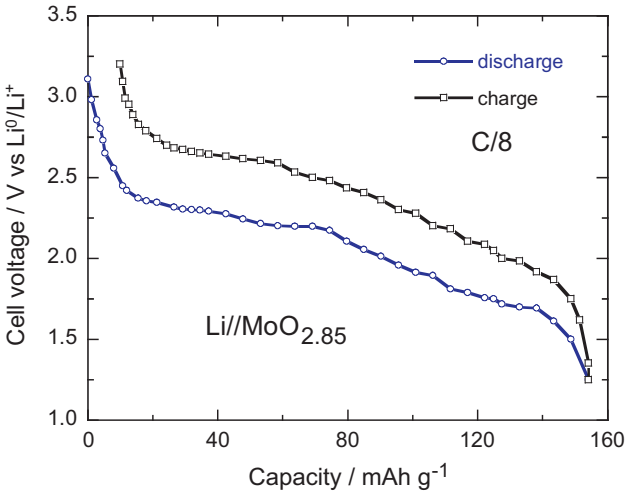

Fig. 11. Discharge–charge-profile of the Li//$MoO_{2.8}$ cell cycled in the potential range 1.2–3.2 V at C/8 rate. The electrode was $MoO_{2.8}$ powders synthesized by solid-state reaction of the molybdic acid MoO_3–H_2O. The electrolyte was 1 mol L^{-1} $LiPF_6$ in 1:1 EC/DMC.

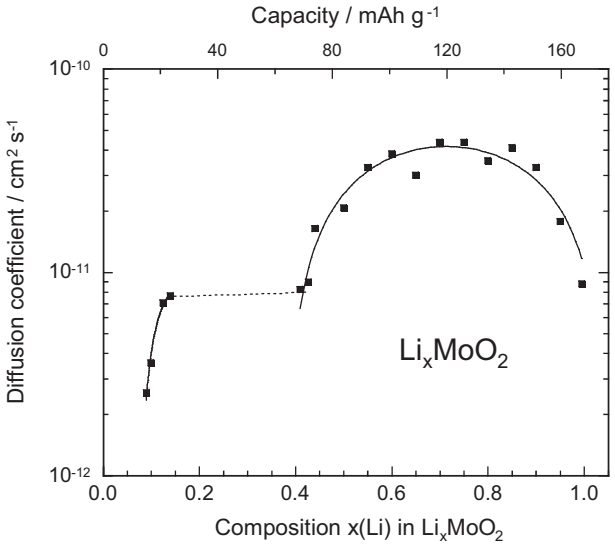

Fig. 12. Evolution of the chemical diffusion coefficient of Li^+ ions in the Li_xMoO_2 cathode material as a function of the composition x.

in the case of $LiVO_2$, in which migration of vanadium ions into the positions formerly occupied by Li was evidenced [29].

In a study of non-stoichiometric Mo oxides having monoclinic structure shear-related to MoO_3, we have examined the Li insertion into $MoO_{2.85}$ powders synthesized by solid-state reaction of the molybdic acid MoO_3–H_2O. Fig. 11 represents the discharge–charge-profile of the Li//$MoO_{2.85}$ cell cycled in the potential range 1.2–3.2 V at C/8 rate. The electrolyte was 1 mol L^{-1} $LiPF_6$ in 1:1 EC/DMC. The lithium insertion occurs with a profile similar to that of the Li//$LiMoO_2$ cell (voltage plateau followed by S-shape curve), but at much lower potential in the range 3.0–1.2 V that is attributed to the higher valence state of molybdenum in $MoO_{2.85}$. This compound can be assigned the Mo valence distribution $Mo^{6+}{}_3Mo^{5+}{}_2$. If reversible lithium incorporation produced all Mo^{4+}, the expected lithium uptake would be 8/5 (=1.6) Li/Mo; a value close to that measured by electrochemical titration (Fig. 11). The lower potential of Li/$MoO_{2.85}$ cell with respect to Li/$LiMoO_2$ cell has already been noticed in Ref. [30]. These authors have reported for $MoO_{2.8}$ an open-circuit voltage 3.1 V vs. Li/Li^+ and a voltage plateau at ca. 2.2 V at small x. These properties are linked to the different crystal chemistry of the Magéli phase with the framework structure based on mixed networks of polyhedra described in [31], and the resulting different electronic structure.

The kinetic parameters of Li^+ ions in $LiMoO_2$ have been estimated using the conventional galvanostatic intermittent titration technique (GITT) for the short time/small current pulse regime [32,33]. Assuming that the transport phenomena in oxides are dominated by Li ions and electrons, the self-diffusion coefficient D_{Li} can be expressed as a product of the diffusion coefficient D_0, the electronic transference number t_e, and the thermodynamic factor of the lithium W [33]. As $LiMoO_2$ is predominantly an electronic conductor, $t_e \approx 1$, so that:

$$D_{Li} = D_0 W = D_0 \frac{\partial \ln(a\mathrm{Li})}{\partial \ln(c\mathrm{Li})} = D_0 \left(-\frac{F}{RT}\frac{xdV}{dx}\right) \quad (5)$$

where R is the gas constant, F the Faraday constant, and T the absolute temperature. The derivative voltage term $(-dV/dx)$ was calculated from the voltage–composition curve shown in Fig. 9. The Faradaic yield $x = 0.9$ was estimated from practical capacity delivered by the Li//$LiMnO_2$ cell. Fig. 12 shows the evolution of the chemical diffusion coefficient of Li^+ ions in the Li_xMoO_2 cathode material as a function of the composition x. Results show that the diffusion coefficients for the $LiMoO_2$ electrode are in the range of 10^{-12}–10^{-10} $cm^2\ s^{-1}$ leading to a diffusion coefficient $D_0 = 2 \times 10^{-12}$ $cm^2\ s^{-1}$. As Li ions are extracted from the host, the initial increase of D_{Li} is attributed to the intercalation process which is partly controlled by the number of ion occupancies in the lattice. For $x > 0.5$, the graph displays a discontinuity that is due to the two-phase system, which behaves with a front diffusion process. The apparent decrease for further Li removal is due to the variation of the term W. These results compare very well with the diffusion coefficients reported in the literature for the $LiCoO_2$ [34–36].

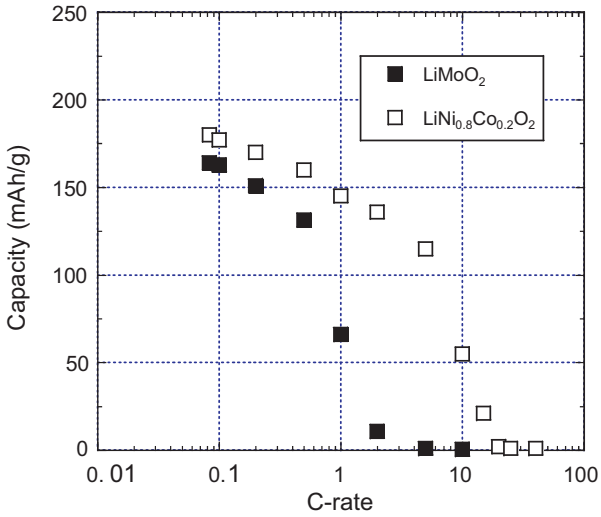

Fig. 13. Ragone plot for Li//$LiMoO_2$ cells recorded at the 5th cycle. Data obtained for the layered $LiNi_{0.8}Co_{0.2}O_2$ cathode are shown for comparison.

The electrochemical tests were carried out at different C-rates to investigate the capabilities of the $LiMoO_2$ cathode material. Fig. 13 shows the Ragone plot recorded at the 5th cycle. Data obtained for the layered $LiNi_{0.8}Co_{0.2}O_2$ cathode are shown for comparison. It is obvious that the monoclinic $LiMoO_2$ lattice is less favourable as cathode material than the layer $LiNi_{0.8}Co_{0.2}O_2$ material. It exhibited almost no capacity at 2C due to the low kinetics of Li^+ ions and the structural destabilisation.

4. Concluding remarks

In this work, we have synthesized and characterized the $LiMoO_2$ compound. The low-temperature growth procedure provides microcrystalline powders with an elongated shape. The careful study of the structure using long-range and local probes has shown that $LiMoO_2$ crystallizes in the monoclinic system with $C2/m$ space group instead of the rhombohedral $R\bar{3}m$ symmetry reported previously. The electrochemical tests show that the voltage profile is related to the two sites occupied by Li ions that are energetically non-equivalent.

References

[1] M. Wakihara, Mater. Sci. Eng. R 33 (2001) 109.
[2] C.M. Julien, Mater. Sci. Eng. R 40 (2003) 47.
[3] D.G. Kellerman, Russian Chem. Rev. 70 (2001) 777.
[4] T.A. Hewston, B.L. Chamberland, J. Phys. Chem. Solids 48 (1987) 97.
[5] A.R. Amstrong, P.G. Bruce, Nature (London) 381 (1996) 499.
[6] T. Ohzuku, Lithium Batteries, New Materials, Developments and Perspectives, Elsevier, Amsterdam, 1993, p. 239.
[7] C.-K. Huang, S. Crouch-Baker, R.A. Huggins, J. Electrochem. Soc. 135 (1988) 408.
[8] C. Julien, G.A. Nazri, Solid State Ionics 68 (1994) 111.
[9] T. Tsumura, M. Inagaki, Solid State Ionics 104 (1997) 183.
[10] O.I. Lebedev, V. Caignaert, B. Raveau, N. Pop, F. Gozzo, G. Van Tendeloo, V. Pralong J., Solid State Chem. 184 (2011) 790.
[11] G. Guzman, B. Yebka, J. Livage, C.M. Julien, Solid State Ionics 86–88 (1996) 407.
[12] S.J. Hibble, I.D. Fawcett, A.C. Hannon, Inorg. Chem. 36 (1997) 1749.
[13] J. Barker, M.Y. Saidi, J.L. Swoyer, Electrochem, Solid State Lett. 6 (2003) A252.
[14] J. Barker, M.Y. Saidi, J.L. Swoyer, Solid State Ionics 158 (2003) 261.
[15] L.E. Aleandri, R.E. McCarley, Inorg. Chem. 27 (1988) 1041.
[16] R.E. McCarley, K.H. Lii, P.A. Edwards, L. Brough J., Solid State Chem. 57 (1985) 17.
[17] C.M. Julien, Ionics 5 (1999) 351.
[18] M. Ghedira, D.C. Do, M. Marezio J., Solid State Chem. 59 (1985) 159.
[19] A. Ōya, M. Kasahara, H. Ohashi, S. Ōtani, J. Am. Ceram. Soc. 74 (1991) 1439.
[20] E. Antolini, Mater. Res. Bull. 32 (1997) 9.
[21] E. Antolini, E. Zhecheva, Mater. Lett. 35 (1998) 380.
[22] C. Julien, Solid State Ionics 136–137 (2000) 887.
[23] W.G. Fataley, F.R. Dollish, N.T. McDevitt, F.F. Bentley, Infrared Raman Selection Rules for Molecular and Lattice Vibrations: The Correlation Method, Wiley-Interscience, New York, 1972.
[24] C.M. Julien, M. Massot, Mater. Sci. Eng. B 100 (2003) 69.
[25] L.S. Cahill, S.-C. Yin, A. Samoson, I. Heinmaa, L.F. Nazar, G.R. Goward, Chem. Mater. 17 (2005) 6560.
[26] D. Zeng, J. Cabana, J. Bréger, W.-S. Yoon, C.P. Grey, Chem. Mater. 19 (2007) 6277.
[27] W.S. Yoon, C.P. Grey, M. Balasubramanian, X.Q. Yang, D.A. Fischer, McBreen, Electrochem. Solid State Lett. 7 (2004) A53.
[28] R.D. Shannon, Crystallogr. Acta A 32 (1976) 751.
[29] L.A. de Picciotto, M.M. Thackeray, W.L.F. David, P.G. Bruce, J.B. Goodenough, Mater. Res. Bull. 19 (1984) 1497.
[30] M. Pasquali, G. Pistio, F. Rodante, Solid State Ionics 6 (1982) 319.
[31] L. Kihlborg, Arkiv. Kem. 21 (1963) 471.
[32] W. Weppner, R. Huggins J., Solid State Chem. 22 (1977) 297.
[33] B. Yebka, C. Julien, Solid State Ionics 90 (1996) 141.
[34] H. Xia, L. Lu, G. Ceder, J. Power Sources 159 (2006) 1422.
[35] Y.H. Rho, K. Kanamura, J. Electrochem. Soc. 151 (2004) A1406.
[36] S.B.##M.O. Tang, Lai L. Lu, J. Alloy Compd. 449 (2008) 300.